Research Square

Preprints are preliminary reports that have not undergone peer review.
They should not be considered conclusive, used to inform clinical practice,
or referenced by the media as validated information.

Chemical diversity of bilin species defines the chiroptical landscape of phytochromes

Andreas Winkler

andreas.winkler@tugraz.at

Graz University of Technology https://orcid.org/0000-0001-6221-9671

Oliver Eder

Graz University of Technology https://orcid.org/0000-0003-4439-1616

Chongyao Wei

TU Dortmund University

Marie Reißenbüchel

Graz University of Technology

Igor Schapiro

TU Dortmund University

Article

Keywords:

Posted Date: May 15th, 2026

DOI: https://doi.org/10.21203/rs.3.rs-9404820/v1

License: This work is licensed under a Creative Commons Attribution 4.0 International License.
Read Full License

Additional Declarations: There is **NO** Competing Interest.

Abstract

Phytochromes are widespread red/far-red light-sensing photoreceptors across several kingdoms of life that enable organisms to adapt their physiology to changing light environments. Major evolutionary transitions, from proteobacteria to cyanobacteria, algae and plants, imposed selective pressure on these proteins to diversify their spectral properties through changes in bilin cofactor preference. This adaptation coincided with a structural relocation of a cysteine residue, the covalent cofactor attachment site, from the N-terminal segment (NTS) to the GAF domain. Here, using the model protein *Is*PadC, we demonstrate how the shift from biliverdin- to phycocyanobilin-binding phytochromes modulates spectroscopic signatures while retaining overall functionality. We further resolve the long-standing question of divergent circular dichroism behavior between NTS_{Cys} and GAF_{Cys} phytochromes through a combination of wet-lab experiments and quantum chemical calculations. Contrary to a widely accepted model, we show that the geometric characteristics of the red-light-activated bilins follow a uniform mechanism across all classical phytochrome lineages. Spectral diversity, instead, arises from the chemical properties of the preferred bilin influenced by subtle structural deviations at the alternative attachment sites. These insights resolve a fundamental debate in phytochrome biology, demonstrate conserved functionality across different bilin species and provide a structural roadmap for color-tuning of phytochrome-based optogenetic tools.

Introduction

Phytochromes are a diverse family of red/far red-light sensing proteins found in a wide range of organisms[1]. By integrating the light quality in the red/far-red regime, phytochromes allow organisms to trigger specific adaptive responses from shade avoidance in plants[2], to virulence[3] and fruiting body induction[4] in bacteria, to depth-dependent photosynthesis acclimation in marine diatoms[5]. Light signal integration of classical phytochromes relies on different bilin cofactors and their embedding in the context of a photosensory module (PSM), a conserved NTS/NTE (N-terminal segment/N-terminal element), PAS (Period/ARNT/Single-minded), GAF (cGMP phosphodiesterase/Adenylyl cyclase/FhlA), PHY (phytochrome specific) domain architecture (Fig. 1)[1].

Interestingly, distinct lineages of phytochromes have evolved diverging bilin cofactor preferences. Specifically, bacteriophytochromes (BphPs) and fungal phytochromes bind biliverdin (BV) whereas their cyanobacterial or plant phytochrome counterparts favor the more reduced phycocyanobilin (PCB) or phytochromobilin (PΦB), respectively[1]. This change in cofactor preference also led to an evolutionary shift in the domain position of the covalent attachment site[6]. While BV allows covalent attachment to a cysteine in the NTS preceding the PAS domain (NTS_{Cys}), PCB/PΦB typically feature a cysteine in the GAF domain (GAF_{Cys}) (Fig. 1)[1, 6, 1]. However, in both prototypical NTS_{Cys} and GAF_{Cys} phytochromes, a highly conserved, elaborate interaction network of GAF domain residues stabilizes the covalently bound bilin cofactor in similar dark-adapted (DA) *ZZZssa* geometries[1, 7]. Additionally, a protrusion of the PHY

domain, the so-called PHY tongue, and the NTS/NTE co-define the chemical environment of the cofactor[8, 9] (Fig. 1) and thus its spectral properties.

In prototypical phytochromes like *Is*PadC, the red-light absorbing state (Pr) has the lowest ground state energy. Accordingly, the light sensing cascade is initiated by red light photon absorption which triggers the photoisomerization of the C15 = C16 double bond of the bilin cofactor[10] (Supplementary Fig. 1). This induces complex rearrangements of the bilin cofactor geometry like the flipping of the D-ring and rotation of the cofactor[11] which in turn leads to a modulation of the bilin's interaction network in the PSM[12]. Lastly, the PHY tongue refolds from a beta hairpin[13] to an α helical[14] conformation[1] and also the NTS/NTE changes its orientation[9, 15–17]. Thus, the so-called phytochrome photocycle involves the transition of the dark-adapted (DA) state to the red light activated state by a progression through complex reaction intermediates[12, 18]. As a sidenote, it is established for many phytochromes that the bilin conformations correspond to an ensemble of Pr and Pfr and/or state-specific subpopulations rather than one defined conformation in both the dark-[19, 20] and red-light-adapted state[14, 21]. Additionally, upon red light illumination, phytochromes like *Is*PadC do not fully convert to the Pfr state but form a mixture of Pr, Pfr and potentially intermediate contributions, which is called photostationary state (PSS)[22]. This behavior is governed by the spectral overlap of the Pr and Pfr states and the extent of the PSS depends on both the ratio between red and far-red light and the relative photocycle rates of Pr◊Pfr versus Pfr◊Pr transitions[1]. This latter transition is additionally a convolution of the meta-stable Pfr state reverting to the dark-adapted Pr state either by far red light illumination or through a light independent mechanism called thermal reversion[1].

While it is established that the bilin dark-adaped (DA) geometries are similar in all phytochromes, there is still a debate over the red light induced conformations in GAF_{Cys} (PCB, PΦB) phytochromes in comparison to the well described NTS_{Cys} (BV) phytochromes. It was previously postulated that the red light induced cofactor geometries would diverge substantially between NTS_{Cys} and GAF_{Cys} phytochromes, especially in the bilin D-ring environment and its either α-facial or β-facial positioning (Fig. 1, middle panel) relative to the plane of the linear tetrapyrrole molecule[23]. This was mainly deduced from strongly diverging CD activities[23] and later supported by structural data derived from NMR experiments and QM/MM simulations[24]. Thus, a "β-slump" mechanism was postulated where the whole D-ring reorients to the bilin β-face (Fig. 1, lower panel) in the Pfr state of GAF_{Cys} phytochromes[23]. Lately, this model was further elaborated to include two distinct photoproduct populations. These would be an alpha facially positioned, deprotonated P_{ALT}[25] conformation proposed to be observed in GAF_{Cys} phytochrome Pfr crystal structures and a true Pfr with the β-slump geometry causing CD sign inversion.

However, a beta slumped Pfr D-ring was contested early on based on the spectroscopic and kinetic data of an artificial PCB-binding Agp1 construct[26]. Moreover, recent XFEL[27] and CryoEM data[16, 17] seems to further disagree with this postulated model. In three independent structural models of PΦB binding GAF_{Cys} phytochromes in their red light induced PSS (Pfr enriched), the bilin D-ring was modelled alpha

facially and thus in the same geometry as in NTS_{Cys} phytochromes (Fig. 1, lower panel). While this structural evidence is compelling, the question of why CD signatures in Pfr of NTS_{Cys} and GAF_{Cys} phytochromes diverge so drastically remains.

To further address this apparent contradiction, we approached this by combining *in vitro* and *in silico* approaches in the model bacteriophytochrome *Is*PadC. Accordingly, specific residues of *Is*PadC were modified to enable binding and covalent attachment of PCB in a GAF_{Cys} mode. Eventually, UV/vis spectroscopy, enzymatic activities and CD data for *Is*PadC BV (NTS_{Cys}) and *Is*PadC PCB C17L L251C (GAF_{Cys}) were measured. In addition, we compared our experimental results with computational CD spectra based on *Is*PadC BV structural data (PDB: 5llw[13]; 6et7[14]) and *in silico* generated *Is*PadC PCB models. Based on our integrative analyses, we propose that all phytochromes feature a similar alpha-facial Pfr D-ring geometry, in line with the structural data discussed above. Furthermore, we show that the chemical differences of the cofactors and the diverging A- and D-ring contributions lead to the observed opposite CD behavior of NTS_{Cys} and GAF_{Cys} phytochromes.

Overall, the work presented expands our understanding of the intricate mechanisms governing red-light sensing phytochromes. The novel insights can inform future efforts depending on a detailed knowledge of the bilin geometry and the energetic landscape. Specifically, these insights could be beneficial for the development and color-tuning of novel optoacoustic imaging probes and other optical reporters derived from phytochromes[28].

Results

UV/vis spectral characterization of IsPadC PCB

During evolution of red-light sensing phytochromes, several lineages adjusted cofactor preferences to enable spectral tuning and/or environmental niche adaptation. BV to PCB/PΦB transitions are typically accompanied by a change in the anchoring position of the bilin from a NTS_{Cys} to a GAF_{Cys} (Fig. 1, Supplementary Fig. 1), respectively. However, the bilin binding-pockets in the GAF domain of diverse phytochromes are still similar enough that the cofactor preference can be interchanged simply by swapping the cysteine position [26]. Thus, *Is*PadC (NTS_{Cys}) was modified to generate a comparable GAF_{Cys} system. Accordingly, an *Is*PadC C17L L251C construct was generated which recreates the structural context of the GAF_{Cys} phytochrome *Syn*Cph1 (PDB: 2vea[30]). This variant was efficiently loaded with PCB (Supplementary Fig. 2B) when co-expressed with the corresponding enzyme machinery[31] and is thus defined as *Is*PadC PCB in this manuscript. Additionally, to account for potentially heterogenous bilin ensembles, we describe experimental in solution data as either dark-adapted (DA) state or red light-activated photostationary state (PSS) as described above.

Importantly, *Is*PadC PCB shows a functional photocycle comparable to *Is*PadC BV (Fig. 2D) with red light-induced bilin isomerization as demonstrated by denaturation experiments (Supplementary Fig. 3).

However, PCB's less extensive conjugated π electron system leads to a blue shift relative to *Is*PadC BV (Fig. 2C). Interestingly, also the Pr Q-band/Soret band ratio increases from roughly 3 (BV) to 3.5 (PCB). In addition, Pfr to Pr thermal reversion is dramatically altered from a mean lifetime of roughly 4 minutes (BV) to more than 24 hours (PCB) (Fig. 2E). Based on this increase in Pfr stability we attempted to address the conformation of the PCB Pfr state by protein crystallization.

Structural characterization of a pseudo-activated IsPadC PCB variant

We previously obtained protein crystals of *Is*PadC in a Pr/Pfr heterodimer architecture[14]. Thus, we set out to reproduce these crystals in the context of *Is*PadC PCB to address potential differences between BV- and PCB-containing phytochromes in their Pfr conformations. To this end, we introduced two amino acid substitutions in the coiled-coil linker region[14] to generate the stabilized stimulating register variant *Is*PadC PCB Reg2 (C17L L251C S505V A526V). Indeed, we obtained crystals under conditions similar to *Is*PadC BV Reg2 and confirmed the presence of a mixed Pr/Pfr content in these crystals using microspectrophotometry (Supplementary Fig. 4, icOS lab, ESRF). However, diffraction of these crystals, even after extensive optimization trials, was limited to > 4 Å. While structure elucidation using molecular replacement was successful, only core regions of the PSM were well defined and the cofactor environment together with the tongue and the NTS did not yield interpretable electron densities.

In order to understand if this was an intrinsic property of *Is*PadC PCB Reg2 or due to the characteristic crystal lattice that is devoid of any tongue involving crystal contacts, we also analyzed the in solution conformational dynamics using hydrogen deuterium exchange coupled to mass spectrometry (HDX-MS). In fact, applying HDX-MS to the *Is*PadC PCB Reg2 variant shows overall higher conformational dynamics in key functional regions of the protein (Supplementary Fig. 5A). Determining the hydrogen to deuterium exchange of backbone amides as a proxy for in-solution protein dynamics, especially the PHY tongue region is markedly more dynamic in the PCB variant versus the wildtype biliverdin binding protein (Supplementary Fig. 5B). Since the PHY tongue is part of the signal integration pathway between the light sensor and the enzymatic output domain, assessing the proteins activity was the next step to address the role of a BV to PCB transition for protein functionality.

Is PadC PCB is a fully functional light activated diguanylate cyclase.

Enzymatic activity of the diguanylate cyclase output can be measured by following GTP to c-di-GMP turnover, hence, we tested if increased PHY tongue dynamics linked to the cofactor exchange would affect the basal enzyme activity in *Is*PadC PCB and if light regulation is still possible. Intriguingly, the PCB variant displays solid inhibition of activity in the dark-adapted (DA) state in combination with activity upregulation upon red light illumination (Fig. 2F). However, the dynamic range is lower in the PCB variant (~ 6-fold) than in the WT context (33-fold), mainly due to a decreased red-light activity relative to *Is*PadC BV. Still, a functional photoreceptor coupled enzyme is retained irrespective of the cofactor linkage. Thus, the core signal transduction mechanism is intact in the PCB construct, already suggesting similar bilin D-ring and tongue properties upon illumination.

Calculated CD spectra reproduce in solution experiments

Having a fully functional PCB-containing system at hand, we wanted to address if our model proteins recapitulate the characteristic in solution differences in the CD signatures of NTS_{Cys} versus GAF_{Cys} phytochromes.

*Is*PadC BV (NTS_{Cys}) behaves as expected for a BV-binding bacteriophytochrome featuring a positive CD signal for the Soret band and a negative contribution in the Q band (Fig. 3A), in line with literature examples[23, 26]. Upon red light illumination, the amplitudes of these bands diminish and a characteristic Pfr shoulder appears at 750 nm (Fig. 3A), reminiscent of the mixed Pr/Pfr states (PSS) of the *Is*PadC absorption spectrum after red light illumination (Fig. 2C).

The dark-adapted (DA) data for the *Is*PadC PCB variant (GAF_{Cys}) displays a subtle positive CD signal contribution in the Q band (Fig. 3B). This behavior is unusual as most previously reported GAF_{Cys} phytochromes feature a negative dark adapted (DA) CD contribution of their Q-bands[23, 26, 25, 32]; however, this observation proved reproducible over multiple protein preparations. In addition, the variant *Is*PadC PCB Reg2 shows similar properties (Supplementary Fig. 6) although some negative contribution can also be observed, which indicates a mixture of PCB states already in the dark-adapted (DA) state.

Importantly, red light activated *Is*PadC PCB undergoes the prominent “sign inversion” and thus a positive CD signal of the Q band (Fig. 3B) as reported for other GAF_{Cys} phytochromes[23, 26, 25, 32]. It is intriguing that the change of cofactor from BV to PCB changes the sign of the rotatory strength in the red light illuminated state. We thus hypothesize that the differences in CD behavior are encoded in the chemical nature of the cofactor and the geometries it can attain based on the position of the covalent attachment site.

To test this hypothesis, CD spectra were calculated *in silico* for structural models of *Is*PadC BV and PCB. For the *Is*PadC BV models, existing PDB entries (Pr: 5llw[13], Pfr: 6et7[14]) were monomerized, truncated after residue 500 to exclude the enzymatic domain while unresolved amino acids in the PHY tongue were added (see Methods and Materials). In parallel, PCB containing models of *Is*PadC were prepared in Coot[33] which was used to introduce the C17L L251C substitutions, the cofactor chemistry changes and the alternative covalent linkage. The dihedral angles of the cofactors within the 4 structural models (BV_{Pr}, BV_{Pfr}, PCB_{Pr}, PCB_{Pfr}) were then optimized by hybrid QM/MM simulations. Since these calculations rely on single bilin geometries, the resulting spectra are denoted as either Pr or Pfr corresponding to idealized dark-adapted (DA) and red light illuminated states, respectively.

The derived calculated excitation energies are systematically shifted (Fig. 3C **+ D**), as already known from benchmark calculations[34]. However, the computational data qualitatively reproduces the trends in the experimental CD spectra (Fig. 3A **+ B**). Specifically, the computational model of the BV Pr state leads to intense signals with a negative sign in the Q-band (Fig. 3C). For the computational BV Pfr model, a single peak with a negative, low amplitude is obtained (Fig. 3C). While, this contrasts the experimental

data featuring a double peak at 708 and 750 nm (Fig. 3A) at first glance, it is just another indication that the experimental in solution data correspond to a mixed Pr/Pfr state (PSS) as indicated by the UV/vis spectra (Fig. 2).

As far as the PCB geometries are concerned, the calculations again suggest a negative contribution for the Pr Q band (Fig. 3D). While this is in line with published phytochrome literature, it is not directly reflected in our experimental data of *Is*PadC PCB, but visible for *Is*PadC PCB Reg2 (Supplementary Fig. 6). However, for the *Is*PadC PCB Pfr model, the theoretical CD spectrum captures the strongly positive oscillator strength in the Q band (Fig. 3D) mirroring the experimental data of *Is*PadC PCB and also other GAF_{Cys} phytochromes. Additionally, the simulated CD spectra also reflect the lower dark-adapted (DA) state rotatory strength of *Is*PadC PCB versus BV even though the configurations of the cofactors are well established to be similar in NTS_{Cys} and GAF_{Cys} phytochromes in their Pr states (Fig. 4A **+ B**, left panel).

It should be specifically noted that our QM/MM optimized models have a similar configuration of BV and PCB also in the Pfr state (Fig. 4A, right panel). Accordingly, the BV versus PCB models used for the calculations feature almost identical D-ring dihedrals and slightly diverging A-ring angles due to the altered covalent binding site. Nevertheless, these configurations (Fig. 4A, right panel) can either lead to a negative rotatory strength (BV) or to a signal with positive sign (PCB) in the simulated CD spectra (Fig. 4B, right panel). This effect is observed when including the protein scaffold in the calculations (Fig. 3A **+ B**) but also prevails when isolating the cofactor geometries and conducting simulations in the “gas phase” (Fig. 4B). Since the CD behavior is comparable between the protein context and gas phase models, we infer that the peak maxima at least in the red wavelength regime is not strongly influenced by removing the interaction network but only the underlying rotatory strengths change slightly (Supplementary Fig. 7).

Overall, the CD signal is proportional to the rotatory strength as computed with the formula $CD \propto\ R = \left|\overrightarrow{\mu}\right| \left|\overrightarrow{m}\right| \bullet\ \cos\theta$. Accordingly, the sign of the rotatory strength and thus the sign of the CD signal are determined by the angle θ between the magnetic and electric transition dipole moments (Fig. 4A). The orientation of these vectors, however, is strongly determined by the specific geometry of the bilin molecule, which in turn is affected by the protein scaffold.

In our calculations, the angle θ is close to 90° for both bilins in Pr and Pfr. However, the nature of the cosine function, which co-defines the rotatory strength, tips the sign to the positive in the Pfr state of PCB (θ = 87.9°, cos(θ) = + 0.036) whereas for the other structures, θ remains above 90° leading to a negative sign (Supplementary Fig. 8). Accordingly, the CD sign behavior is dominated by slight alterations of the transition dipole moments induced by the conformation and chemical configuration of the bilin cofactor.

Influence of A-ring rotation and the conjugated π electron system on CD signatures

To test the influence of A-ring orientation on the transition dipole moments and the CD signal sign, the dihedral angle of the N_A-C4-C5-C6 bonds was rotated *in silico* relative to the plane of the BV and PCB geometries in the gas phase (Fig. 5A **+ B**). Interestingly, the relative rotation of the A-ring by + 20°/-20° has strong implications on the CD sign relative to the original reference geometry of BV (Fig. 5C, ref.). Specifically, CD sign inversion is observed when the A-ring is tilted by -20°. In contrast, A-ring rotation has only negligible effects for PCB regardless of the rotation direction (Fig. 5D). Thus, the A-ring conformation influences CD sign inversion, however, this behavior strongly depends on the conjugation to the rest of the bilin molecule. Accordingly, in PCB the contribution of the rotated A-ring seems to be markedly reduced due to its more reduced A-ring character and hence shows a more strongly D-ring influenced CD signature. Apparently, the change of conjugation on the A-ring in PCB significantly alters the electric and magnetic transition dipole moments.

To further visualize these discrete differences in chemistry and the exact extent of the delocalized π electron systems, molecular orbitals of the BV and PCB optimized geometries were calculated (Supplementary Fig. 9). In both HOMO and LUMO orbital calculations the observed differences in the conjugated π electron are caused by diverging substituents on the A- and D-ring. Specifically, comparing BV and PCB, there is a double or single C3-$C3^1$ bonding character on the A-ring and either a vinyl or an ethyl group on the bilin D-ring, respectively.

To illuminate the influence of these chemical differences, the C3 = $C3^1$ bond on the A-ring and the $C18^2$=$C18^3$ bond on the D-ring of BV were saturated *in silico* by hydrogen addition. As expected, this leads to a blue shift of the spectrum especially in the higher wavelength regime (Fig. 6A) due to the smaller extent of the conjugated system (Fig. 6B). Interestingly, saturation of either double bond is sufficient to induce CD sign inversion in the Pfr geometry of BV (Fig. 6A, right panel). Yet, it should be noted that this effect is more pronounced for the Pfr BV $C18^2$-$C18^3$ dataset. Apparently, with the compensating D-ring contributions gone, the A-ring chemistry and the geometry are enough to tilt the angle between the electric and magnetic transition dipole moments leading to CD sign inversion in the simulations. Summing up, the CD characteristics of bilins depend on the intricate balance of the A- and D-ring chemistry in combination with their relative orientation as governed by the protein scaffold.

Discussion

Following the first CD spectroscopic analyses of NTS_{Cys}/GAF_{Cys} phytochromes, the community was intrigued by the opposite Q band CD activity in the Pfr state. In 2009, it was postulated that this peculiar CD behavior is caused by substantially diverging Pfr D-ring geometries (Fig. 1) between these phytochrome families[23]. Though widely adopted, this model also sparked controversy[26] and might have also led to some confusion in the field. Specifically, many authors would agree with a PCB/PΦB D-ring

where its nitrogen would serve as a marker to identify transient shifts from the alpha to beta facial plane of the molecule. However, the postulated beta slump[23] i.e. a complete reorientation of the D-ring to the beta face (Fig. 1) is, in our opinion, not compatible with the spatial and energetic characteristics of the phytochrome bilin binding pocket. Furthermore, a beta slumped D-ring would presumably not enable identical PHY-tongue interactions and ultimately output domain regulation, however, *Is*PadC PCB still behaves as a *bona fide* red light regulatable enzyme (Fig. 2F).

Additionally, multiple recent GAF_{Cys} Pfr structures unequivocally modeled the Pfr PΦB D-ring alpha facially[27, 16, 17] which is further contrasting the beta slump hypothesis. Thus, we tried to provide an integrative characterization of the CD behavior of NTS_{Cys} versus GAF_{Cys} phytochromes using experimental results for one defined GAF environment in combination with computational modelling. Understanding the intriguing opposite Pfr CD behavior of different bilins in the phytochrome context requires to consider a key parameter influencing CD intensity and sign, the rotatory strength. Being proportional to the CD signal, the rotatory strength is the scalar product of the absolute values of the magnetic (*m*) and electric (*μ*) dipole transition moments and the angle (θ) between these vectors ($CD \propto \ R = \left|\overrightarrow{\mu}\right| \left|\overrightarrow{m}\right| \bullet \ \cos\theta$)[35, 36].

In our quantum chemical calculations, this sign defining angle θ was determined as 90.58° (BV Pfr, cos(θ)= − 0.010) or 87.9° (PCB Pfr, cos(θ) = + 0.036) (Supplementary Fig. 8), a seemingly minute but still impactful difference. Thus, although the modelled Pfr BV and PCB conformations intuitively look very similar, they have opposite CD signs. Apparently, even when assuming a similar geometry between BV and PCB, the differences in chemistries of the A- and D-ring are enough to alter θ and thus not just affect the sign but also the amplitude of the CD signals (Fig. 6).

Interestingly, PΦB is chemically similar to the artificially C3-C3[1] saturated BV where the simulated CD data (Fig. 6) reproduces a peculiar pattern in the literature. Specifically, in all available CD datasets involving PΦB binding GAF_{Cys} phytochromes the amplitude of the sign inverted peak is very weak[32, 37, 38]. When compared to PCB data in the same protein context[32], this would further suggest that also the D-ring substituents can contribute to the sign and amplitude of the CD signal. Overall, when also considering the presented A-ring rotation data it seems that the CD behavior is encoded by both the relative geometry and chemistry of the A- and D-ring.

This is in line with other organic compounds where the CD sign showed strong dependence on slight tilting of substituents which changed the angle θ[39, 36]. In addition, closely related compounds can have CD spectra with opposite signs if substituents induce a diverging relative twist of chromophore groups on the same facial side of the molecule[40]. Accordingly, there are precedents in the literature where CD sign inversion is caused by relatively minute angle differences rather than drastic configurational changes.

We conclude that the diverging CD behavior in NTS_{Cys} versus GAF_{Cys} phytochromes is caused by the differences in the A- and D-ring substituents as well as the specific geometry of the molecule which is induced by the protein scaffold. The differences in the conjugated electron system and its relative orientation would influence the angle θ between the electric and magnetic transition dipole moment which determines the sign of the rotatory strength and thus the behavior of the CD signal.

Admittedly, this model is initially less intuitive than the beta slump hypothesis. Notably, in some instances, CD sign inversion can be induced by the relocation of a chromophore group to the opposite side of a molecules plane for example in photoswitchable azobenzenes[41]. However, multiple studies have raised the concern that, especially in complex molecules, the interpretation of geometries directly from CD spectra should be considered with care[42, 43]. This is especially apparent when multiple chromophore groups change their relative geometry simultaneously which can also lead to complex compensatory effects in the CD spectrum, as seen for example in some chiroptical switches[44].

We would like to additionally stress that only the beginning and the end point of the Pr-to-Pfr photocycle were modeled for the CD spectra calculations. Thus, the exact progression of the CD sign during the photocycle remains elusive. However, we propose that the red light triggered sign inversion in GAF_{Cys} phytochromes requires either late photocycle intermediates or full Pfr formation. This is deduced from the observation that in the GAF_{Cys} phytochrome *Syn*Cph1, only PAS-GAF-PHY constructs show a positive Pfr CD signal whereas in PAS-GAF variants no signal inversion is observed[25]. As proposed elsewhere[9, 45], these PAS-GAF constructs might only reach a Pfr-like state. Thus, CD sign inversion might depend on the full array of structural rearrangements and importantly the protonation/reprotonation events which are the hallmarks of true Pfr formation. In similar vein, the observed pH effect in *Syn*Cph1 PAS-GAF-PHY where at pH 9 no sign inversion is apparent[25] might be caused by the inability of the system to relax to full Pfr upon photoactivation. We thus propose that for CD sign inversion specific geometric and/or chemical requirements need to be fulfilled.

Importantly, in our calculations the angle θ is very close to 90°, thus already small spatial disturbances of the molecule lead to either weak CD signatures or positive signals. This might explain the rare literature occurrences of dark-adapted (DA) state CD spectra with a positive sign in the Q band as published for a CBCR (PCB-GAF3 of RGS)[46] and for the *Syn*Cph1 Y263S PSM variant[47]. At least in the *Syn*Cph1 Y263F PSM structure (PDB: 3ZQ5[47]), removal of the hydroxyl group results in a slightly altered interaction network and a diverging D-ring angle relative to rings B and C[47].

For the *Is*PadC PCB dark-adapted (DA) state CD data, which features a similarly unexpected positive peak in the Q band, a similar phenomenon might occur potentially caused by increased dynamics of the whole cofactor and/or slightly diverging D-ring angles which would skew the angle θ. The exact specifics remain elusive, however, also the well-established Pr cofactor structural heterogeneity in PCB/PΦB binding phytochromes[20, 48, 19] might additionally contribute to this phenomenon. Based on the additional data for *Is*PadC PCB Reg2, clearly an overlay of a positive and a negative signal defines the observed

dark-adapted (DA) state CD signature. Considering the very slow thermal recoveries of the PCB containing *Is*PadC variants and the much stronger positive oscillator strength of the Pfr contributions, the heterogeneity of samples appears to be the easiest explanation. Along this line, it has been demonstrated that experimental CD spectra of cyanobacteriochromes can also be rationalized by a composition of several different bilin structures in the case of AnPixJg2[49].

For the research of phytochrome evolution, this study also provides interesting insights. Recently, an unexpected family of double Cys (NTS_{Cys} + GAF_{Cys}) phytochromes was identified that were proposed to be the "missing link" between NTS_{Cys} and GAF_{Cys} phytochrome families[50]. However, at least in our *in vitro* PadC trials, the functional penalty for exchanging the cysteine position from the NTS to the GAF domain is minute and might be well tolerated in an organism. Additionally, other authors showed that a plant phytochrome can attach BV to GAF_{Cys} and still retain signaling properties, at least in an artificial reporter setup[32]. While we agree that the route over double cysteine intermediates is quite reasonable, in the light of this evidence, we want to suggest that potentially alternative intermediates between NTS_{Cys} and GAF_{Cys} phytochromes were at least theoretically possible.

To conclude, we provide a unifying hypothesis for the CD behavior of NTS_{Cys} versus GAF_{Cys} phytochromes. Specifically, we propose that all prototypical knotted phytochromes feature a bilin Pfr D-ring in an alpha facial position. The CD sign inversion in GAF_{Cys} phytochromes, however, is strongly influenced by the diverging chemistry of BV versus PCB. This is further substantiated by a GAF_{Cys} plant phytochrome binding BV [32], as this variant shows CD sign inversion upon red light illumination[32]. This additionally supports the dependency of CD signatures on specific bilin chemistry rather than altered conformations in the GAF domain. In addition to the chemical differences, also diverging A-ring dihedrals, induced by the location of the cysteine for covalent attachment, and/or slightly different D-ring angles further influence the extent of Pfr Q band CD signatures in phytochromes.

While this model conflicts with MAS NMR data that initially seemed to confirm the beta slump model[24], a discrepancy between X-ray crystallographic data and MAS NMR approaches has also been reported in other phytochromes[51]. The exact origins of such inconsistencies are difficult to rationalize, however, MAS NMR provides more indirect interpretations of local chemical environments based on spectroscopic shifts, whereas crystal structures allow spatial mapping of atomic coordinates, typically rendering them the benchmark for structural features. Re-evaluation of existing data and/or generation of additional datasets for other model phytochromes will resolve this issue in the future. Especially in the light of new structural techniques to address Pfr states in previously elusive phytochromes, this will be an interesting field to follow. Eventually, this scientific discussion will be settled once higher resolution time resolved X-FEL data of GAF_{Cys} phytochromes and/or time resolved circular dichroism data on multiple model systems become available.

Materials and Methods

Cloning, expression, and purification

The wildtype sequence of *Idiomarina* sp. A28L PadC (WP_007419415) was subcloned into the pETM11 vector system as first described in[13]. Point mutations for variants C17L and L251C were introduced via a PCR protocol as described by Liu and Naismith[52]. A list of used primers can be found in **Supplementary Table 1**.

Expression of biliverdin binding protein variants was conducted in the strain BL21 (DE3) recA::ho1 pEcgRNA as published in[53]. This CRISPR modified strain contains a genomically inserted heme oxygenase (HO-1) from Synechocystis sp. PCC6803 for efficient biliverdin-IXα production. For PCB binding constructs, BL21 (DE3) was co-transformed with the respective phytochrome encoding pETM11 vector and the helper plasmid pKT271. As previously described[31], this plasmid encodes two proteins, a heme oxygenase (HO1) and a ferredoxin oxidoreductase (PcyA), and thus the complete machinery for efficient PCB production from heme.

Growing conditions for bacterial cultures involved a non-actinic dim green light environment and LB media (“Lennox”, Roth; 10 g/L Trypton, 5 g/L Yeast extract, 5 g/L NaCl) supplemented with kanamycin (34 µg/mL), 8.5 mM $MgCl_2$ and 0.3 % glucose. When using the helper plasmid pkT271, we additionally supplemented the growing medium with chloramphenicol (30 µg/mL). Cultures were grown at 37 °C at 130 rpm until reaching an optical density of 0.5 followed by addition of δ-aminolevulinic acid (10 µg/mL) and cooling to 18 °C for 30 minutes. Upon addition of isopropyl-β-D-thiogalactopyranoside (IPTG, 0.25 mM), cultures were incubated at 130 rpm and 18°C for 14-18 hours.

We harvested bacterial suspensions by centrifugation for 15 min. at 5,000 RCF and 8 °C. The resulting pellets were either frozen and stored at -20 °C or directly resuspended in lysis buffer (50 mM HEPES pH 7.0, 500 mM NaCl, 2 mM $MgCl_2$, 10 mM Imidazol, 100 µg/mL lysozyme, 100 µg/mL DNase, EDTA-free protease inhibitor). The resuspended solution was sonified (4x 5 min, 50W, Labsonic LU, 0.7s duty cycle, ice water cooling) for cell disruption followed by clearing of the lysate by centrifugation (39,000 RCF, 4°C, 1h). *Is*PadC BV and PCB holoprotein were purified in a gravity flow setup utilizing a Ni^{2+} NTA matrix (Ni SepharoseTM 6 Fast Flow). On the column pre-equilibrated with lysis buffer, the cell lysate was added followed by 10 column volumes wash buffer (50 mM HEPES pH 7.0, 500 mM NaCl, 2 mM $MgCl_2$, 50 mM imidazol). The protein of interest was removed by elution buffer addition (50 mM HEPES pH 7, 500 mM NaCl, 2 mM $MgCl_2$, 250 mM Imidazol). Eluted protein fractions were concentrated using centrifugal filters (Amicon MW cut-off 30,000 Da, 4000 RCF) followed by a size exclusion step using a Superdex 200 Increase 10/300GL column equilibrated in size exclusion buffer (10 mM HEPES pH 7.0, 500 mM NaCl, 2 mM $MgCl_2$). Using centrifugal filters as described above, monodisperse peak fractions were concentrated, flash frozen in liquid nitrogen and stored at -80 °C.

Ultraviolet-visible (UV-vis) absorption spectroscopy

UV/vis spectra were recorded using a Specord 200 plus spectrophotometer with 1 nm spacing, with a scan rate of 200 nm/s, and an integration time of 5 ms. Protein samples were diluted to 2 µM in 500 µL size exclusion buffer (see above) and measured in a quartz cuvette. Protein samples were either measured in the dark-adapted state or illuminated for 1 minute with red light to populate a Pfr enriched photostationary state (PSS, BV: 660 nm, PCB 630 nm, 20 mW/cm2, Thorlabs).

For thermal reversion, the same sample preparation steps and general photometer settings were used. The sample was Illuminated for 1 minute with red light (BV: 660 nm, PCB: 630 nm). Then the absorbance was measured at two wavelengths (BV: 705/750 nm, PCB: 650/700 nm) at specific time intervals. These time intervals were chosen to guarantee a marginal activating effect of the measuring light while a sufficient amount of datapoints for the non-linear fit should be achieved.

CD spectroscopy

CD spectra were collected on a Chirascan Plus spectropolarimeter (Applied Photophysics) using 1 mm quartz cuvettes at a temperature of 20 °C. A wavelength scan from 770-270nm was conducted with a step size of 1 nm, a bandwidth of 2 nm and the time per point set to 0.1 s. Samples with concentrations of 100-200 µM were either kept in darkness or illuminated 2 min. with red light (BV: 660 nm, PCB: 630 nm). Buffer measurements were subtracted from the raw data and the resulting traces were smoothed by averaging 2-3 scans.

Steady-state enzymatic activity

Enzymatic activity experiments of *Is*PadC BV and PCB were conducted according to a protocol described previously[54]. Briefly, concentrated protein stocks were thawed and freshly purified by size exclusion chromatography according to the protocol above since aggregates were shown to skew activity results in pretrials.

The proteins of interest were diluted to 0.2 µM in reaction buffer (10mM Hepes pH=7.0, 500 mM NaCl, 50 mM $MgCl_2$) and equilibrated at 20 °C in the dark. For dark-adapted reactions, samples were then illuminated at 780 nm for 5 min., followed by a 13 min. incubation in darkness. Subsequently, dark reactions were handled under safe light conditions (BV: indirect green light, PCB: indirect blue light). Red light reactions were pre-illuminated for 1 min (BV: 660 nm, PCB: 630 nm) followed by continuous illumination during the experiment.

The enzyme reaction was initiated by mixing 100 µL of the protein solution with 100 µL of 100 µM GTP (99 %; ROTH, Karlsruhe, Germany) solution in reaction buffer. Thus, a batch reaction was created from which 35 µL solution can be retrieved at given time intervals (dark-adapted series: 10 s, 1 min., 3 min. ,6 min., 20 min.; red light series 10 s, 20 s, 1 min., 3 min. and 6 min). Note that each batch reaction was created in triplicates for *Is*PadC BV or PCB and dark-adapted or red light, respectively.

The retrieved 35 µL were added to 10 µL of a 250 mM EDTA (pH=8) solution to quench the reaction followed by immediate denaturation at 96 °C for 1 minute. The finished reactions were transiently stored on ice. We then centrifuged samples at 16,110 g for 15 min to remove precipitated protein. The supernatant was transferred to HPLC glass vial insets and analyzed on a Prontosil C18 reversed-phase HPLC column with an aqueous mobile phase buffer (10mM Hepes pH=7.0, 0.5 M NaCl, 50 mM $MgCl_2$) and MetOH in a 88/12 percent mixture under isocratic conditions with the column department being heated to 25 °C. A UV/vis detector was used to determine relative peak areas of GTP and c-di-GMP. Subsequently, the % c-di-GMP (product) concentration in each sample was calculated and plotted against time to calculate a linear fit using the first three timepoints. The standard deviation of the triplicates of each timepoint was considered to calculate the weighted standard error of the linear fit which is shown as the error indicator above the enzymatic activity bars in the figure. Finally, the enzymatic activity was plotted in a bar chart with the unit (µmol product) / (min. x µmol *Is*PadC dimer). As a sidenote, none of the datasets showed formation of the reaction intermediate pppGpG.

Intact mass spectrometry

The following experiments were conducted according to a protocol described previously[54]. In brief, protein samples were diluted in SEC buffer (see above) to 10 µM. 2 µL of this solution was loaded on a Shim-pack Scepter C4-300 (G) column and washed with 1 % ACN/ 0.1 % formic acid. The sample was eluted with a ACN gradient (1-95 %) which transferred the samples to an Impact II ESI-Q-TOF (Bruker) mass spectrometer. Protein signals were analyzed in the DataAnalysis tool (Bruker) by integration and deconvolution using the maximum entropy function.

Hydrogen deuterium exchange mass spectrometry (HDX-MS)

The HDX-MS workflow was conducted as described previously[55]. Briefly, the proteins of interest were diluted in size exclusion buffer (see above) to a concentration of 40 µM. For each series, e.g. *Is*PadC BV red light, 3 reaction tubes (1.5 mL) were prepared with 5 µL protein solution each followed by flash freezing in liquid nitrogen.

For each of the 3 reaction tubes, the same sample treatment was conducted to generate triplicates for each timepoint. The reaction tube was quickly thawed and equilibrated for 1 minute at 20 °C in a heating block. During this equilibration and the following labeling step, the samples were kept under non activating light conditions (dark-adapted, BV: indirect green light, PCB: indirect blue light). To start the reaction, 95 µL labeling buffer (10mM HEPES pD 7.0, 150 mM NaCl, 10 mM $MgCl_2$) was added. From this mix, 16 µL were retrieved consecutively from the same reaction tube at specific timepoints (10 s, 45 s, 180 s, 900 s 3600 s) and quenched immediately by pipetting into a new tube containing 16 µL quench buffer (200 mM ammonium formate, pH 2.6). The sample was then flash frozen in liquid nitrogen. Samples were processed by thawing the 32 µL mix by addition of 80 µL ice cold quenching buffer followed by immediate injection of 100 µL into a cooled HPLC system.

Directly after injection, the protein samples were proteolytically digested on an immobilized pepsin column (BEH Enzymate, Waters) at 10 °C with a flow rate of 0.3 mL/min. Using a C18 trap column (Shim-pack GISS-HP(G), Shimadzu), the resulting peptide fragments were desalted. Afterwards, the peptides were separated on a C18 reversed-phase column (Shim-pack Arata Peptide, Shimadzu) utilizing a 4.25 min acetonitrile gradient (from 10% to 45%) with a constant amount of 0.6% (v/v) formic acid. The eluting peptides were electrospray ionized and measured in an Impact II ESI-Q-TOF (Bruker) mass spectrometer. For data analysis, data files were exported in the mzxml format whereas deuterium incorporation was quantitated in the Hexicon 2 software package[56]. Sample carry over was characterized by injection of blanks and was thus determined to be less than 10 %. In addition, the characteristics of fully exchanging peptides were utilized to estimate a back exchange fraction of around 30%. Find additional in-depth description and tips for HDX-MS workflows in the literature by Fuchs and Winkler et al.,[57]. HDX-MS statistics for the shown datasets are provided in Supplementary Table 2.

Preparation of structural models for *in silico* calculations

The dark-adapted structure of *Is*PadC BV was retrieved from PDB:5llw[13] truncated after residue 500, monomerized and missing atoms were filled in using the protein preparation wizard in the Schrodinger tool kit. The Pfr enriched structure of *Is*PadC BV was similarly retrieved from PDB:6et7[14] (chain A), truncated after residue 500 and monomerized. However, missing atoms were added by creating models in the SWISS-MODEL webserver[58, 59].

The dark-adapted model of *Is*PadC PCB was initially created using the PyMol Molecular Graphics System (Version 2.2 Schrödinger, LLC) by overlaying the GAF domains of *Is*PadC BV (5llw[13]) with the dark-adapted PCB binding phytochrome *Syn*Cph1 (2vea[30]). The PCB cofactor was copied to the 5llw model and exported. In the software Coot[33], the substitutions C17L and L251C together with the alternative covalent binding mode of the GAF_{Cys} was introduced. For the Pfr model of *Is*PadC PCB, the SWISS-MODEL generated dataset of *Is*PadC BV Pfr was utilized as template. The chemistry of the cofactor, the C17L and L251C substitutions and the alternative covalent binding mode of the GAF_{Cys} were again introduced in the software suit Coot.

Hybrid Quantum Mechanics/Molecular Mechanics simulation

The structural models were prepared according to the section above and further processed using the tleap plugin of AMBER[60] to add missing hydrogens. The protonation state of each residue was considered under the condition of pH = 7.0. The system was then solvated in a rectangular water box with 12 Å between the boundary and the system. The protein was described using the ff14SB force field[61], and the chromophore was described using previously published parameters[49].

The geometries were initially minimized using classic molecular mechanics to resolve clashes resulting from the crystal structures and added hydrogen atoms. Then, QM/MM optimization was performed on the structures from the previous step. The QM region consisted of the entire chromophore and the Cys

residue truncated at Cβ-Cα (as described in [62]), with the Cα residue replaced by a hydrogen atom. The QM region was described using DFT at the B3LYP[63] level of theory, with D3 dispersion correction and Becke–Johnson damping (BJ)[64].

The QM/MM excited state calculation was performed for 15 excited states, using the same QM region and TD-CAM-B3LYP[65] functional which was previously benchmarked for bilins[34]. All the excited state calculation results were analyzed using the Multiwfn[66] program to generate the HOMO and LUMO orbitals.

To validate the effect of the dihedral angle of the A-ring on rotary strength, a gas-phase quantum chemical calculation was performed inspired by previous work[67]. To this end, the QM region was isolated from the QM/MM simulation described above. In addition, the propionates were also truncated. As the propionates are not conjugated with the tetrapyrrole rings, they don't contribute to the excitation in the visible range. In the calculation, the dihedral angle of the A-ring was rotated by 10° (or -10°) five times in a so-called unrelaxed scan. For each rotation, the excitation energy was calculated using TD-CAM-B3LYP/6-31G* with D3BJ dispersion correction as mentioned above.

As the main difference between BV and PCB is the double bond on the A-ring and D-ring side chains, another calculation was performed to compare the extent of conjugation in the first excitation. The C3-C3[1] double bonds on rings A and D, respectively, were separately replaced with single bonds by adding hydrogen, in order to cancel the conjugation between the side chain and the rings. The replaced bonds were reoptimized using B3LYP/6-31G* with D3BJ. Then excited state calculation was performed for 15 excited states using TD-CAM-B3LYP/6-31G* with D3BJ dispersion correction.

Declarations

Acknowledgements:

We would like to thank Philipp Pelzmann and Christoph Schaffer for their continuous technical support. We acknowledge the European Synchrotron Radiation Facility (ESRF) for provision of synchrotron radiation facilities under proposal ID MX-2529 and for access to the icOS microspectrophotometry facilities. We thank Antoine Royant and Sylvain Engilberge for assistance and support during the experiments. O.M.E. is supported by the Austrian Science Fund (FWF) grant 10.55776/DOC130 and was trained within the framework of the PhD program Biomolecular Structures and Interactions (BioMolStruct). This research was funded in whole, or in part, by the Austrian Science Fund (FWF) (10.55776/P32022 and 10.55776/PAT6932824 to A.W). I.S. acknowledges support from the Swiss National Science Foundation (SNF) through the grant no. CRSII5_213507 and the Deutsche Forschungsgemeinschaft (DFG, German Research Foundation) under Germany's Excellence Strategy – EXC 2033 – 390677874 – RESOLV. For open access purposes, the authors have applied a CC BY public copyright license to any author accepted manuscript version arising from this submission.

References

1. Hughes, J., and Winkler, A. (2024). New Insight Into Phytochromes: Connecting Structure to Function. Annual review of plant biology *75,* 153–183. 10.1146/annurev-arplant-070623-110636.
2. Franklin, K.A., and Whitelam, G.C. (2005). Phytochromes and shade-avoidance responses in plants. Annals of botany *96,* 169–175. 10.1093/aob/mci165.
3. Bonomi, H.R., Toum, L., Sycz, G., Sieira, R., Toscani, A.M., Gudesblat, G.E., Leskow, F.C., Goldbaum, F.A., Vojnov, A.A., and Malamud, F. (2016). Xanthomonas campestris attenuates virulence by sensing light through a bacteriophytochrome photoreceptor. EMBO reports *17,* 1565–1577. 10.15252/embr.201541691.
4. Woitowich, N.C., Halavaty, A.S., Waltz, P., Kupitz, C., Valera, J., Tracy, G., Gallagher, K.D., Claesson, E., Nakane, T., and Pandey, S., et al. (2018). Structural basis for light control of cell development revealed by crystal structures of a myxobacterial phytochrome. IUCrJ *5,* 619–634. 10.1107/S2052252518010631.
5. Duchêne, C., Bouly, J.-P., Pierella Karlusich, J.J., Vernay, E., Sellés, J., Bailleul, B., Bowler, C., Ribera d'Alcalà, M., Falciatore, A., and Jaubert, M. (2025). Diatom phytochromes integrate the underwater light spectrum to sense depth. Nature *637,* 691–697. 10.1038/s41586-024-08301-3.
6. Rockwell, N.C., and Lagarias, J.C. (2019). Phytochrome evolution in 3D: deletion, duplication, and diversification. The New phytologist. 10.1111/nph.16240.
7. Wagner, J.R., Brunzelle, J.S., Forest, K.T., and Vierstra, R.D. (2005). A light-sensing knot revealed by the structure of the chromophore-binding domain of phytochrome. Nature *438,* 325–331. 10.1038/nature04118.
8. Anders, K., Daminelli-Widany, G., Mroginski, M.A., Stetten, D. von, and Essen, L.-O. (2013). Structure of the Cyanobacterial Phytochrome 2 Photosensor Implies a Tryptophan Switch for Phytochrome Signaling. J Biol Chem *288,* 35714–35725. 10.1074/jbc.M113.510461.
9. Buhrke, D., Gourinchas, G., Müller, M., Michael, N., Hildebrandt, P., and Winkler, A. (2020). Distinct chromophore-protein environments enable asymmetric activation of a bacteriophytochrome activated diguanylate cyclase. The Journal of biological chemistry *295,* 539–551. 10.1074/jbc.RA119.011915.
10. Velazquez Escobar, F., Kneip, C., Michael, N., Hildebrandt, T., Tavraz, N., Gärtner, W., Hughes, J., Friedrich, T., Scheerer, P., and Mroginski, M.A., et al. (2020). The Lumi-R Intermediates of Prototypical Phytochromes. The journal of physical chemistry. B *124,* 4044–4055. 10.1021/acs.jpcb.0c01059.
11. Yang, X., Kuk, J., and Moffat, K. (2009). Conformational differences between the Pfr and Pr states in *Pseudomonas aeruginosa* bacteriophytochrome. Proc Natl Acad Sci U S A *106,* 15639–15644. 10.1073/pnas.0902178106.
12. Carrillo, M., Pandey, S., Sanchez, J., Noda, M., Poudyal, I., Aldama, L., Malla, T.N., Claesson, E., Wahlgren, W.Y., and Feliz, D., et al. (2021). High-resolution crystal structures of transient

intermediates in the phytochrome photocycle. Structure (London, England : 1993). 10.1016/j.str.2021.03.004.

13. Gourinchas, G., Etzl, S., Göbl, C., Vide, U., Madl, T., and Winkler, A. (2017). Long-range allosteric signaling in red light-regulated diguanylyl cyclases. Sci Adv *3,* e1602498. 10.1126/sciadv.1602498.
14. Gourinchas, G., Heintz, U., and Winkler, A. (2018). Asymmetric activation mechanism of a homodimeric red light regulated photoreceptor. eLife *7,* e34815. 10.7554/eLife.34815.
15. Li, H., Burgie, E.S., Gannam, Z.T.K., Li, H., and Vierstra, R.D. (2022). Plant phytochrome B is an asymmetric dimer with unique signalling potential. Nature *604,* 127–133. 10.1038/s41586-022-04529-z.
16. Wang, Z., Wang, W., Zhao, D., Song, Y., Lin, X., Shen, M., Chi, C., Xu, B., Zhao, J., and Deng, X.W., et al. (2024). Light-induced remodeling of phytochrome B enables signal transduction by phytochrome-interacting factor. Cell *187,* 6235-6250.e19. 10.1016/j.cell.2024.09.005.
17. Jia, H., Guan, Z., Ding, J., Wang, X., Tian, D., Zhu, Y., Zhang, D., Liu, Z., Ma, L., and Yin, P. (2025). Structural insight into PIF6-mediated red light signal transduction of plant phytochrome B. Cell Discov *11,* 51. 10.1038/s41421-025-00802-3.
18. Hildebrandt, P. (2023). Vibrational Spectroscopy of Phytochromes. Biomolecules *13.* 10.3390/biom13061007.
19. Song, C., Essen, L.-O., Gärtner, W., Hughes, J., and Matysik, J. (2012). Solid-state NMR spectroscopic study of chromophore-protein interactions in the Pr ground state of plant phytochrome A. Molecular plant *5,* 698–715. 10.1093/mp/sss017.
20. Velázquez Escobar, F., Lang, C., Takiden, A., Schneider, C., Balke, J., Hughes, J., Alexiev, U., Hildebrandt, P., and Mroginski, M.A. (2017). Protonation-Dependent Structural Heterogeneity in the Chromophore Binding Site of Cyanobacterial Phytochrome Cph1. The journal of physical chemistry. B *121,* 47–57. 10.1021/acs.jpcb.6b09600.
21. Velazquez Escobar, F., Stetten, D. von, Günther-Lütkens, M., Keidel, A., Michael, N., Lamparter, T., Essen, L.-O., Hughes, J., Gärtner, W., and Yang, Y., et al. (2015). Conformational heterogeneity of the Pfr chromophore in plant and cyanobacterial phytochromes. Frontiers in molecular biosciences *2,* 37. 10.3389/fmolb.2015.00037.
22. Butler, W.L., Hendricks, S.B., and Siegelman, H.W. (1964). ACTTON SPECTRA OF PHYTOCHROME IN VITRO *. Photochem & Photobiology *3,* 521–528. 10.1111/j.1751-1097.1964.tb08171.x.
23. Rockwell, N.C., Shang, L., Martin, S.S., and Lagarias, J.C. (2009). Distinct classes of red/far-red photochemistry within the phytochrome superfamily. PNAS *106,* 6123–6127. 10.1073/pnas.0902370106.
24. Song, C., Mroginski, M.A., Lang, C., Kopycki, J., Gärtner, W., Matysik, J., and Hughes, J. (2018). 3D Structures of Plant Phytochrome A as Pr and Pfr From Solid-State NMR: Implications for Molecular Function. Frontiers in plant science *9,* 498. 10.3389/fpls.2018.00498.
25. Rockwell, N.C., and Lagarias, J.C. (2025). Circular dichroism spectroscopy reveals multiple phytochrome photoproducts in equilibrium. Photochem Photobiol Sci, 1–21. 10.1007/s43630-025-

00763-2.

26. Borucki, B., Seibeck, S., Heyn, M.P., and Lamparter, T. (2009). Characterization of the covalent and noncovalent adducts of Agp1 phytochrome assembled with biliverdin and phycocyanobilin by circular dichroism and flash photolysis. Biochemistry *48,* 6305–6317. 10.1021/bi900436v.
27. Nagano, S., Stetten, D. von, Guan, K., Chen, P.-Y., Song, C., Barends, T., Weiss, M.S., Feiler, C.G., Dörner, K., and Diego Martinez, I. de, et al. (2025). Pr and Pfr structures of plant phytochrome A. Nat Commun *16,* 5319. 10.1038/s41467-025-60738-w.
28. Tang, K., Beyer, H.M., Zurbriggen, M.D., and Gärtner, W. (2021). The Red Edge: Bilin-Binding Photoreceptors as Optogenetic Tools and Fluorescence Reporters. Chemical reviews *121,* 14906–14956. 10.1021/acs.chemrev.1c00194.
29. Burgie, E.S., Wang, T., Bussell, A.N., Walker, J.M., Li, H., and Vierstra, R.D. (2014). Crystallographic and Electron Microscopic Analyses of a Bacterial Phytochrome Reveal Local and Global Rearrangements during Photoconversion. J Biol Chem *289,* 24573–24587. 10.1074/jbc.M114.571661.
30. Essen, L.O., Mailliet, J., and Hughes, J. (2008). The structure of a complete phytochrome sensory module in the Pr ground state. Proc Natl Acad Sci U S A *2008/09/19,* 14709–14714. 10.1073/pnas.0806477105.
31. Mukougawa, K., Kanamoto, H., Kobayashi, T., Yokota, A., and Kohchi, T. (2006). Metabolic engineering to produce phytochromes with phytochromobilin, phycocyanobilin, or phycoerythrobilin chromophore in Escherichia coli. FEBS Lett *2006/02/07,* 1333–1338. 10.1016/j.febslet.2006.01.051.
32. Möglich, A., Yi, C., Golonka, D., Meier, S., Tang, K., Ihalainen, J., and Zurbriggen, M. (2025). Commutability of Bilin Chromophores in Plant Phytochromes.
33. Emsley, P., Lohkamp, B., Scott, W.G., and Cowtan, K. (2010). Features and development of Coot. Acta crystallographica. Section D, Biological crystallography *66,* 486–501. 10.1107/S0907444910007493.
34. Wiebeler, C., and Schapiro, I. (2019). QM/MM Benchmarking of Cyanobacteriochrome Slr1393g3 Absorption Spectra. Molecules (Basel, Switzerland) *24.* 10.3390/molecules24091720.
35. Bedi, A., Schwartz, G., Hananel, U., Manor Armon, A., Shioukhi, I., Markovich, G., and Gidron, O. (2023). The effect of axial and helical chirality on circularly polarized luminescence: lessons learned from tethered twistacenes. Chemical communications (Cambridge, England) *59,* 2011–2014. 10.1039/d2cc07074j.
36. Hirose, T., Inoue, Y., Hasegawa, J., Higashiguchi, K., and Matsuda, K. (2014). Investigation on CD inversion at visible region caused by a tilt of the π-conjugated substituent: theoretical and experimental approaches by using an asymmetric framework of diarylethene annulated isomer. The journal of physical chemistry. A *118,* 1084–1093. 10.1021/jp4122694.
37. Bjorling, S.C., Zhang, C.F., Farrens, D.L., Song, P.S., and Kliger, D.S. (1992). Time-resolved circular dichroism of native oat phytochrome photointermediates. J. Am. Chem. Soc. *114,* 4581–4588. 10.1021/ja00038a020.

38. Kroes, H.H. (1968). Reversible changes in the circular dichroism of phytochrome during photoisomerisation of the pigment. Biochemical and Biophysical Research Communications *31,* 877–883. 10.1016/0006-291x(68)90533-0.

39. Takaishi, K., Muranaka, A., Kawamoto, M., and Uchiyama, M. (2012). Photoinversion of cisoid/transoid binaphthyls. Organic letters *14,* 276–279. 10.1021/ol203053q.

40. Padula, D., and Pescitelli, G. (2018). How and How Much Molecular Conformation Affects Electronic Circular Dichroism: The Case of 1,1-Diarylcarbinols. Molecules (Basel, Switzerland) *23.* 10.3390/molecules23010128.

41. Takaishi, K., and Kawamoto, M. (2011). Synthesis and conformation of substituted chiral binaphthyl-azobenzene cyclic dyads with chiroptical switching capabilities. Molecules (Basel, Switzerland) *16,* 1603–1624. 10.3390/molecules16021603.

42. Berova, N., Di Bari, L., and Pescitelli, G. (2007). Application of electronic circular dichroism in configurational and conformational analysis of organic compounds. Chemical Society reviews *36,* 914–931. 10.1039/b515476f.

43. Padula, D., Di Bari, L., and Pescitelli, G. (2016). The "Case of Two Compounds with Similar Configuration but Nearly Mirror Image CD Spectra" Refuted. Reassignment of the Absolute Configuration of N-Formyl-3',4'-dihydrospiroindan-1,2'(1'H)-pyridine. The Journal of organic chemistry *81,* 7725–7732. 10.1021/acs.joc.6b01416.

44. Petermayer, C., and Dube, H. (2018). Circular Dichroism Photoswitching with a Twist: Axially Chiral Hemiindigo. Journal of the American Chemical Society *140,* 13558–13561. 10.1021/jacs.8b07839.

45. Nagano, S., Guan, K., Shenkutie, S.M., Feiler, C., Weiss, M., Kraskov, A., Buhrke, D., Hildebrandt, P., and Hughes, J. (2020). Structural insights into photoactivation and signalling in plant phytochromes. Nat Plants *6,* 581–588. 10.1038/s41477-020-0638-y.

46. Chen, Y., Zhang, J., Luo, J., Tu, J.-M., Zeng, X.-L., Xie, J., Zhou, M., Zhao, J.-Q., Scheer, H., and Zhao, K.-H. (2012). Photophysical diversity of two novel cyanobacteriochromes with phycocyanobilin chromophores: photochemistry and dark reversion kinetics. The FEBS journal *279,* 40–54. 10.1111/j.1742-4658.2011.08397.x.

47. Mailliet, J., Psakis, G., Feilke, K., Sineshchekov, V., Essen, L.-O., and Hughes, J. (2011). Spectroscopy and a high-resolution crystal structure of Tyr263 mutants of cyanobacterial phytochrome Cph1. Journal of molecular biology *413,* 115–127. 10.1016/j.jmb.2011.08.023.

48. Song, C., Psakis, G., Lang, C., Mailliet, J., Gärtner, W., Hughes, J., and Matysik, J. (2011). Two ground state isoforms and a chromophore D-ring photoflip triggering extensive intramolecular changes in a canonical phytochrome. PNAS *108,* 3842–3847. 10.1073/pnas.1013377108.

49. Rao, A.G., Wiebeler, C., Sen, S., Cerutti, D.S., and Schapiro, I. (2021). Histidine protonation controls structural heterogeneity in the cyanobacteriochrome AnPixJg2. Physical chemistry chemical physics : PCCP *23,* 7359–7367. 10.1039/d0cp05314g.

50. Yang, H.W., Song, J.-Y., Song, J.-J., Kim, Y.W., Rockwell, N.C., Kim, W., Kim, H., Lagarias, J.C., and Park, Y.-I. (2025). Dual-Cys bacteriophytochromes: intermediates in cyanobacterial phytochrome

evolution? FEBS J. 10.1111/febs.17395.

51. Burgie, E.S., Mickles, A.J., Luo, F., Miller, M.D., and Vierstra, R.D. (2024). Crystal Structure of the Photosensory Module from a PAS-Less Cyanobacterial Phytochrome as Pr Shows a Mix of Dark-Adapted and Photoactivated Features. The Journal of biological chemistry, 107369. 10.1016/j.jbc.2024.107369.
52. Liu, H., and Naismith, J.H. (2008). An efficient one-step site-directed deletion, insertion, single and multiple-site plasmid mutagenesis protocol. BMC biotechnology *2008/12/06,* 91. 10.1186/1472-6750-8-91.
53. Eder, O.M., Jančić, M., and Winkler, A. (2026). Strategies for Coexpression of Bilin-Producing Enzymes in Escherichia coli. Methods in molecular biology (Clifton, N.J.) *2970,* 29–50. 10.1007/978-1-0716-4791-2_3.
54. Tran, Q.H., Eder, O.M., and Winkler, A. (2024). Dynamics-driven allosteric stimulation of diguanylate cyclase activity in a red light-regulated phytochrome. The Journal of biological chemistry *300,* 107217. 10.1016/j.jbc.2024.107217.
55. Eder, O.M., Totaro, M.G., Minnich, S., Oberdorfer, G., and Winkler, A. (2025). Integrating protein sequence design and evolutionary sequence conservation to uncover spectral tuning sites in red-light photoreceptors. Structure *33,* 1916-1929.e3. 10.1016/j.str.2025.07.018.
56. Lindner, R., Lou, X., Reinstein, J., Shoeman, R.L., Hamprecht, F.A., and Winkler, A. (2014). Hexicon 2: automated processing of hydrogen-deuterium exchange mass spectrometry data with improved deuteration distribution estimation. J. Am. Soc. Mass Spectrom. *25,* 1018–1028. 10.1007/s13361-014-0850-y.
57. Fuchs, M., and Winkler, A. (2026). Hydrogen-Deuterium Exchange Coupled to Mass Spectrometry-Based Analysis of Phytochrome Photoreceptors. Methods in molecular biology (Clifton, N.J.) *2970,* 245–265. 10.1007/978-1-0716-4791-2_15.
58. Arnold, K., Bordoli, L., Kopp, J., and Schwede, T. (2006). The SWISS-MODEL workspace: a web-based environment for protein structure homology modelling. Bioinformatics (Oxford, England) *22,* 195–201. 10.1093/bioinformatics/bti770.
59. Waterhouse, A., Bertoni, M., Bienert, S., Studer, G., Tauriello, G., Gumienny, R., Heer, F.T., Beer, T.A.P. de, Rempfer, C., and Bordoli, L., et al. (2018). SWISS-MODEL: homology modelling of protein structures and complexes. Nucleic acids research *46,* W296-W303. 10.1093/nar/gky427.
60. Case, D.A., Aktulga, H.M., Belfon, K., Cerutti, D.S., Cisneros, G.A., Cruzeiro, V.W.D., Forouzesh, N., Giese, T.J., Götz, A.W., and Gohlke, H., et al. (2023). AmberTools. Journal of chemical information and modeling *63,* 6183–6191. 10.1021/acs.jcim.3c01153.
61. Maier, J.A., Martinez, C., Kasavajhala, K., Wickstrom, L., Hauser, K.E., and Simmerling, C. (2015). ff14SB: Improving the Accuracy of Protein Side Chain and Backbone Parameters from ff99SB. Journal of chemical theory and computation *11,* 3696–3713. 10.1021/acs.jctc.5b00255.
62. Nag, P., Wei, C., Mackintosh, M.J., and Schapiro, I. (2026). Computational Protocols to Study Phytochromes. Methods in molecular biology (Clifton, N.J.) *2970,* 121–135. 10.1007/978-1-0716-

4791-2_8.

63. Becke, A.D. (1993). Density-functional thermochemistry. III. The role of exact exchange. The Journal of chemical physics *98,* 5648–5652. 10.1063/1.464913.
64. Grimme, S., Antony, J., Ehrlich, S., and Krieg, H. (2010). A consistent and accurate ab initio parametrization of density functional dispersion correction (DFT-D) for the 94 elements H-Pu. The Journal of chemical physics *132,* 154104. 10.1063/1.3382344.
65. Yanai, T., Tew, D.P., and Handy, N.C. (2004). A new hybrid exchange–correlation functional using the Coulomb-attenuating method (CAM-B3LYP). Chemical Physics Letters *393,* 51–57. 10.1016/j.cplett.2004.06.011.
66. Lu, T. (2024). A comprehensive electron wavefunction analysis toolbox for chemists, Multiwfn. The Journal of chemical physics *161*. 10.1063/5.0216272.
67. Rockwell, N.C., Njuguna, S.L., Roberts, L., Castillo, E., Parson, V.L., Dwojak, S., Lagarias, J.C., and Spiller, S.C. (2008). A second conserved GAF domain cysteine is required for the blue/green photoreversibility of cyanobacteriochrome Tlr0924 from Thermosynechococcus elongatus. Biochemistry *47,* 7304–7316. 10.1021/bi800088t.

Figures

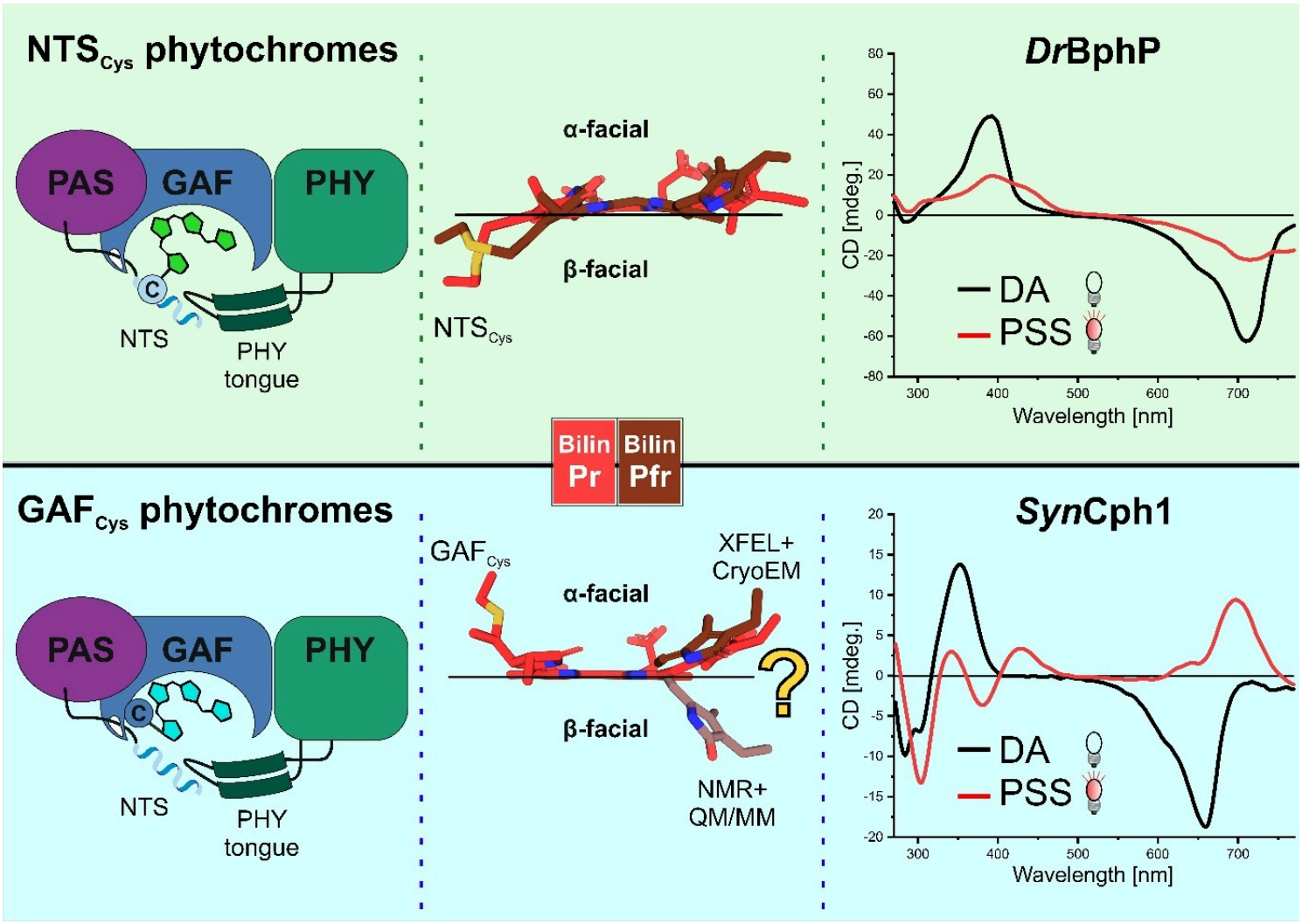


Figure 1

Overview of central light sensing aspects of NTS$_{Cys}$ and GAF$_{Cys}$ phytochromes. Scheme of the PAS-GAF-PHY photosensory module (PSM, left panel). The GAF domain stabilizes the bilin cofactor which can be either covalently linked to a NTS$_{Cys}$ (light blue) or a GAF$_{Cys}$. (dark blue). In the shown phytochromes, the cofactor is biliverdin (green) and phycocyanobilin (turquoise), respectively. The colors reflect their diverging absorption characteristics. The chemical environment of the cofactor is additionally co-defined by the NTS and the PHY tongue. Bilin geometries upon Pr (red) versus Pfr (brown) formation in side view (middle panel). In NTS$_{Cys}$ phytochromes, it is well established that the D-ring remains on the alpha facial side in both the Pr [13, 14, 29, 30] and Pfr state[14], respectively. In GAF$_{Cys}$ phytochromes, the Pr conformation of the D-ring is also alpha facial while for the Pfr state conflicting structural models exist. While previous data (NMR+QM/MM) suggested a beta facial Pfr D-ring[24], more recent data (XFEL+CryoEM) shows alpha facial stabilization of the D-ring[16, 17, 27]. Note that the A/B/C-ring atoms of the two conflicting structural datasets are not shown to aid visibility. Representative CD behavior of NTS$_{Cys}$ and GAF$_{Cys}$ phytochromes (right panel). While in NTS$_{Cys}$ phytochromes there is a change in amplitude of the CD signal between the Pr and Pfr state, in GAF$_{Cys}$ phytochromes the sign of

the Q band inverts between the states. The *Dr*BphP CD data was isolated from an online available figure[23] using the AI tool “Starry Digitizer” and was subsequently denoised. The *Syn*Cph1 data was obtained from ref. [25] and subsequently denoised.

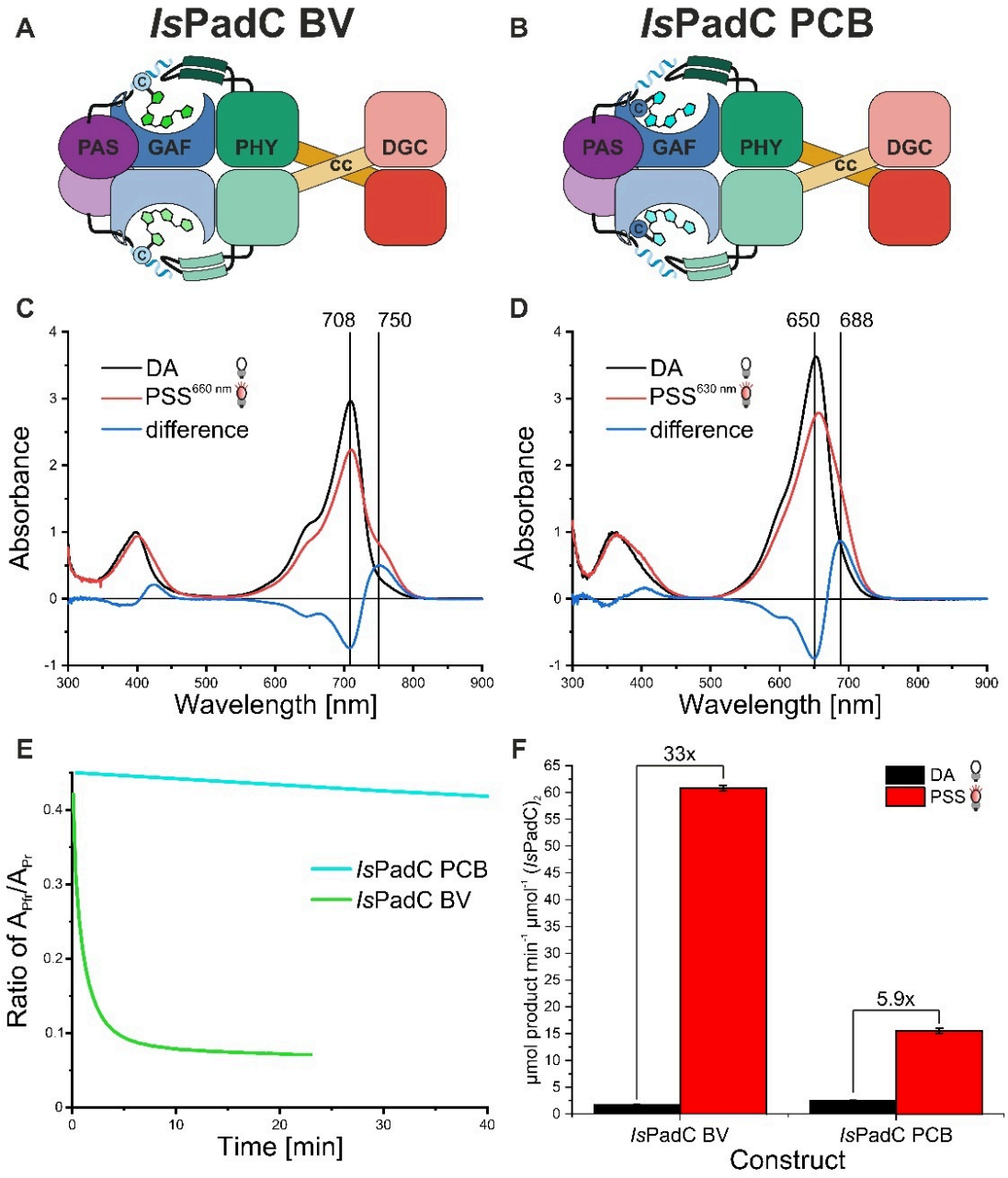


Figure 2

Biochemical characterization of *Is*PadC BV and *Is*PadC PCB. A+B) Schematic representation of the dimeric assemblies of *Is*PadC BV and *Is*PadC PCB. Note the diverging cysteine linkage points of either NTS_{Cys} (BV) and GAF_{Cys} (PCB). In addition to the conserved PAS-GAF-PHY domain array, the dimer has a coiled coil (cc, yellow) linker that translates light signals to a diguanylate cyclase (DGC/GGDEF, red) output domain. C+D) UV/vis characterization of *Is*PadC BV and *Is*PadC PCB. The dark-adapted state (DA) is shown as a black line whereas the red light induced photostationary state (BV: $PSS^{660\ nm}$, PCB: $PSS^{630\ nm}$) is depicted in red. Black vertical lines highlight the maxima and minima of the difference spectrum (PSS minus DA) in blue. Spectra are scaled to 1 according to their Pr Soret band maximum (BV: 398 nm, PCB: 357 nm). E) Thermal reversion kinetics of *Is*PadC BV and PCB. After population of the PSS with red light, the ratios of the difference spectrum maximum/minimum are plotted against time (BV: $A_{750\ nm}/A_{705\ nm}$, PCB: $A_{700\ nm}/A_{650\ nm}$). F) Specific activity per dimer for *Is*PadC BV and PCB in the dark-adapted (DA) state versus the red light induced PSS. Substrate turnover was measured at a GTP concentration of 50 µM for both dark- and light-adapted conditions. The calculated fold changes of the dark-adapted (DA) versus red light illuminated PSS samples are depicted over the brackets. For each bar, specific activity was determined from a linear fit of a time course experiment where each time point was measured in triplicates. The error bars show the weighted standard error of this linear fit.

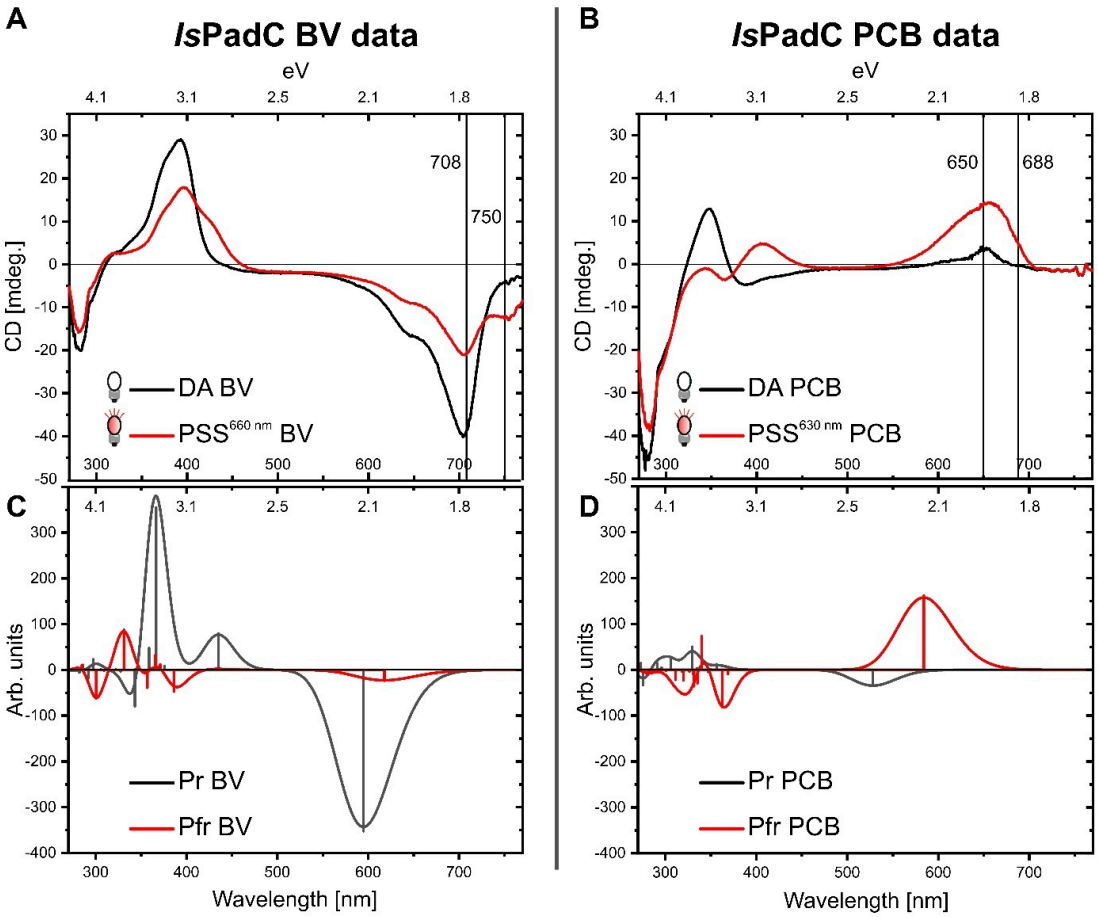


Figure 3

***In vitro* and *in silico* characterization of CD optical activity of *Is*PadC variants.** A+B) Experimentally determined CD traces of *Is*PadC BV and PCB in the dark-adapted (DA, black) and red light induced PSS (red). Black vertical lines indicate the maxima and minima of the UV/vis difference spectrum as determined in **Figure 2**. C+D) Computational CD spectra calculated from QM/MM optimized geometries

of *Is*PadC BV and PCB in the Pr (black) or Pfr (red) conformation. Discrete CD rotatory strengths are overlayed with a gaussian function (FWHM = 0.25 eV) to generate a continuous CD spectrum.

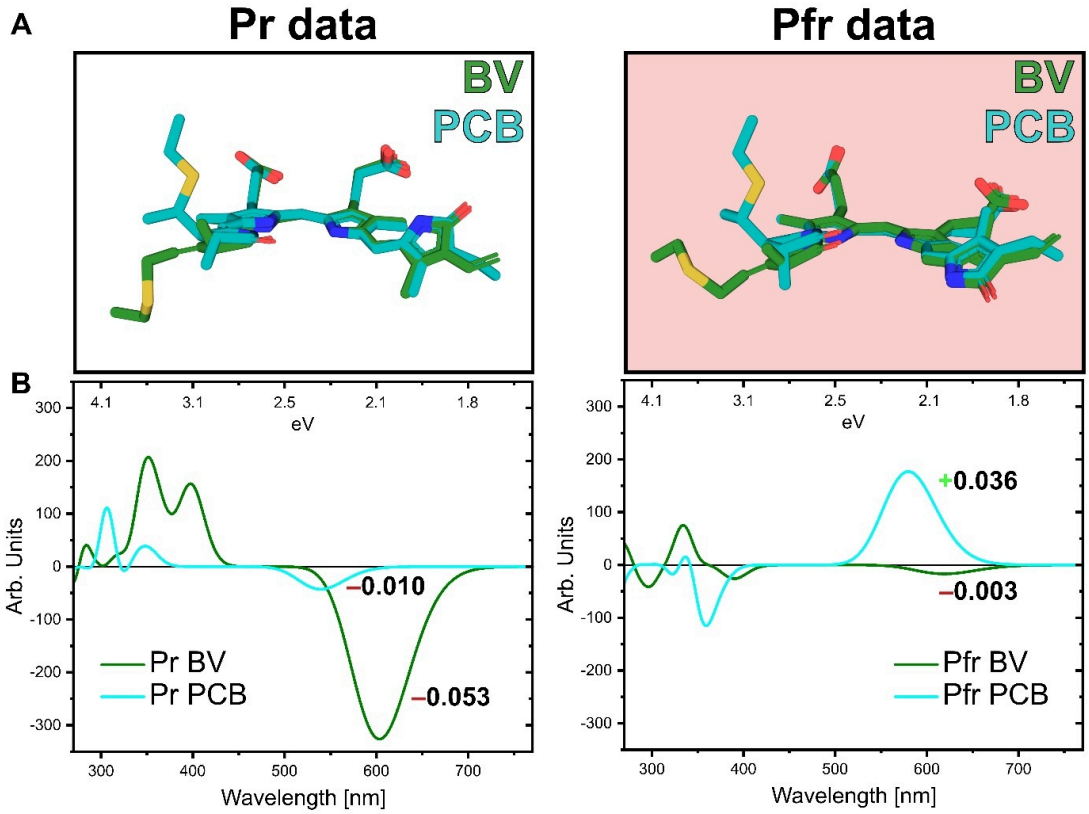


Figure 4

The CD sign is influenced by the relative orientation of transition dipole moments. A) Overlay of the QM/MM optimized structures of BV (green) and PCB (turquoise) in Pr (left) versus Pfr (right). B) *In silico*

calculated CD spectra of bilins in the gas phase. Note that the general CD behavior is reminiscent of the in-protein calculations in **Figure 3**as mostly the relative intensities in the lower wavelength regions changes. These intensities are proportional to the electric and magnetic transition dipole moment vectors while the sign of the traces depends on cosine of the angle θ between these vectors. These cos(θ) values are depicted as insets (e.g. -0.010). See also Supplementary Figure 8.

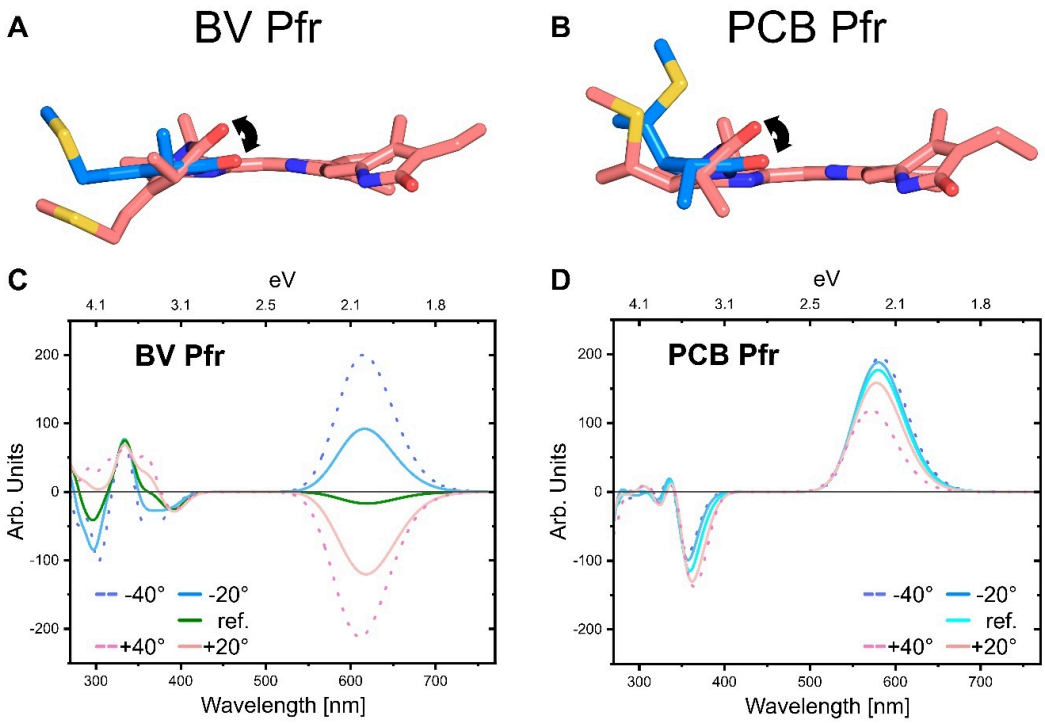


Figure 5

***In silico* rotation of the bilin A-ring and calculated CD spectra.** A+B) Visualization of Pfr bilin geometries with modified A-ring dihedral angles (black arrows). Shown are the -20° (blue) and +20° (salmon) rotations in the gas phase relative to the original reference QM/MM optimized geometry (not shown). C+D) Calculated CD spectra of gas phase bilins with modified A-ring orientations. In both panels, calculated CD spectra for the original reference QM/MM bilin pose (BV green, PCB cyan), the -40° (dark blue, dashed line), the -20° (blue), the +20° (salmon) and the +40° (pink, dashed line) rotated A-ring geometries are displayed.

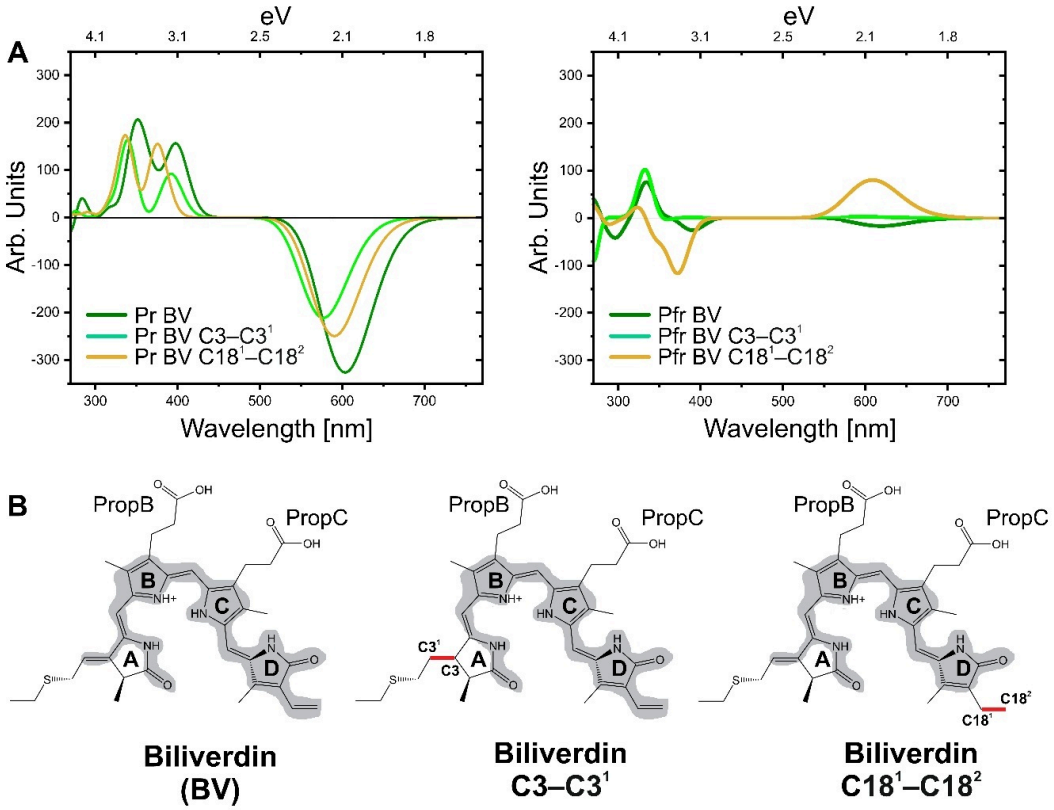


Figure 6

The delocalized electron system affects the CD signal *in silico*. A) Calculated CD spectra of bilin geometries in the gas phase. The CD spectra were calculated for the Pr (left) and the Pfr (right) geometry which were isolated from the protein context (5llw: Pr, 6et7, chain A: Pfr). Spectra are shown for different *in silico* conjugated electron systems with biliverdin (BV, dark green) and saturation of the double bond of the A-ring (BV C3-C3^1, turquoise) and D-ring (BV C18^1-C18^2, gold), respectively. B) Chemical structures of compounds used to calculate the CD spectra above. Note the different extents of the conjugated π electron systems as highlighted in grey. Differences in double bond saturation are additionally highlighted in red.

Supplementary Files

This is a list of supplementary files associated with this preprint. Click to download.

- Supplementaryinformation.pdf